

1 **Source-Resolved Volatility and Oxidation State Decoupling in**
2 **Wintertime Organic Aerosols in Seoul**

3
4 Hwajin Kim^{1,2,*}, Jiwoo Jeong¹, Jihye Moon¹, Hyun Gu Kang^{2,3}

5 ¹Department of Environmental Health Sciences, Graduate School of Public Health, Seoul National University, 08826 Seoul,
6 South Korea

7 ²Institute of Health and Environment, Graduate School of Public Health, Seoul National University, 08826 Seoul, South Korea

8 ³Now at Multiphase Chemistry Department, Max Planck Institute for Chemistry, 55128 Mainz, Germany

9 *Correspondence to:* Hwajin Kim (khj0116@snu.ac.kr)

10 **Abstract.**

11 Organic aerosols (OA) are key components of wintertime urban haze, but the relationship between their oxidation
12 state and volatility—critical for understanding aerosol evolution and improving model predictions—remains poorly
13 constrained. While oxidation–volatility decoupling has been observed in laboratory studies, field-based evidence
14 under real-world conditions is scarce, particularly during severe haze episodes. This study presents a field-based
15 investigation of OA sources and their volatility characteristics in Seoul during a winter haze period, using a
16 thermodenuder coupled with a high-resolution time-of-flight aerosol mass spectrometer (HR-ToF-AMS).

17 Positive matrix factorization resolved six OA factors: hydrocarbon-like OA, cooking, biomass burning, nitrogen-
18 containing OA (NOA), less-oxidized oxygenated OA (LO-OOA), and more-oxidized OOA (MO-OOA). Despite
19 having the highest oxygen-to-carbon ratio (~1.15), MO-OOA exhibited unexpectedly high volatility, indicating a
20 decoupling between oxidation state and volatility. We attribute this to fragmentation-driven aging and autoxidation
21 under stagnant conditions with limited OH exposure. In contrast, LO-OOA showed lower volatility and more
22 typical oxidative behavior.

23 Additionally, NOA—a rarely resolved factor in wintertime field studies—was prominent during cold, humid, and
24 stagnant conditions and exhibited chemical and volatility features similar to biomass burning OA, suggesting a
25 shared combustion origin and meteorological sensitivity.

26 These findings provide one of the few field-based demonstrations of oxidation–volatility decoupling in ambient
27 OA and highlight how source-specific properties and meteorology influence OA evolution. The results underscore
28 the need to refine OA representation in chemical transport models, especially under haze conditions.

29

30 **Keywords:** Organic aerosol volatility, HR-ToF-AMS, Thermodenuder, elemental ratios, aging, fragmentation

31 **1 Introduction**

32 Atmospheric aerosols affect both human health and the environment by reducing visibility (Ghim et al., 2005; Zhao
33 et al., 2013) and contributing to cardiovascular and respiratory diseases (Hamanaka et al., 2018; Manisalidis et al.,
34 2020). In addition, aerosols play a significant role in climate change by scattering or absorbing solar radiation and
35 modifying cloud properties (IPCC AR6). Among the various aerosol components—including sulfate, nitrate,
36 ammonium, chloride, crustal materials, and water—organic aerosols (OA) are particularly important to characterize,
37 as they account for 20–90% of submicron particulate matter (Zhang et al., 2007). Identifying OA sources and
38 understanding their behavior are critical for effective air quality management; however, this is particularly
39 challenging due to the vast diversity and dynamic nature of OA compounds, which originate from both natural and
40 anthropogenic sources. Unlike inorganic aerosols, organic aerosols (OAs) evolve continuously through complex
41 atmospheric reactions, influenced by emission sources, meteorological conditions, and aerosol properties (Jimenez
42 et al., 2009; Hallquist et al., 2009; Robinson et al., 2007; Donahue et al., 2006; Ng et al., 2010; Cappa and Jimenez,
43 2010).

44 Volatility is a key parameter for characterizing organic aerosol (OA) properties, as it governs gas-to-particle
45 partitioning behavior and directly influences particle formation yields (Sinha et al., 2023). The classification of OA
46 species based on their volatility—from extremely low-volatility (ELVOC) to semi-volatile (SVOC) and intermediate-volatility
47 (IVOC) compounds—is central to the conceptual framework of secondary OA (SOA) formation and growth (Donahue et al.,
48 2006). It also affects atmospheric lifetimes and human exposure by determining how long aerosols remain
49 suspended in the atmosphere (Glasius and Goldstein, 2016). Therefore, accurately capturing OA volatility is
50 essential for improving predictions of OA concentrations and their environmental and health impacts. However,
51 chemical transport models often significantly underestimate OA mass compared to observations (Matsui et al.,
52 2009; Jiang et al., 2012; Li et al., 2017), largely due to incomplete precursor inventories and simplified treatment
53 of processes affecting OA volatility. For instance, aging—through oxidation reactions such as functionalization
54 and fragmentation—can significantly alter volatility by changing OA chemical structure (Robinson et al., 2007;
55 Zhao et al., 2016). Early volatility studies primarily utilized thermal denuders (TD) coupled with various detection
56 instruments to investigate the thermal properties of bulk OA (Huffman et al., 2008). The subsequent coupling of TD with the
57 Aerosol Mass Spectrometer allowed for component-resolved volatility measurements, providing critical, quantitative insight
58 into the properties of OA factors (e.g., SV-OOA vs. LV-OOA) across different regions (Paciga et al., 2016; Cappa and Jimenez,
59 2010). These component-resolved volatility data are often used to constrain the Volatility Basis Set (VBS)—the current state-
60 of-the-art framework for modeling OA partitioning and evolution (Donahue et al., 2006). However, a limitation in many field
61 studies is that the TD-AMS thermogram data are rarely translated into quantitative VBS distributions for individual OA factors,

62 which limits their direct use in chemical transport models. Furthermore, the volatility of OOA during extreme haze conditions,
63 where the expected inverse correlation between oxidation (O:C) and volatility can break down (Jimenez et al., 2009), remains
64 poorly characterized, particularly in East Asia's highly polluted winter environments. A recent study in Korea further
65 highlighted the importance of accounting for such processes when interpreting OA volatility under ambient
66 conditions (Kang et al., 2023). Given its central role in OA formation, reaction, and atmospheric persistence,
67 volatility analysis is critical for bridging the gap between measurements and model performance.

68 Traditionally, due to the complexity and variability of OA, the oxygen-to-carbon (O:C) ratio has been used as a
69 proxy for estimating volatility. In general, higher O:C values indicate greater oxidation and lower volatility
70 (Jimenez et al., 2009). Accordingly, many field studies classify oxygenated OA (OOA) into semi-volatile OOA
71 (SV-OOA) and low-volatility OOA (LV-OOA) based on their O:C ratios (Ng et al., 2010; Huang et al., 2010; Mohr
72 et al., 2012). However, this relationship is not always straightforward. Fragmentation during oxidation can increase
73 both O:C and volatility simultaneously, disrupting the expected inverse correlation (Jimenez et al., 2009). In
74 laboratory experiments, yields of highly oxidized SOA have been observed to decrease due to fragmentation (Xu
75 et al., 2014; Grieshop et al., 2009). These findings suggest that while O:C can offer useful insights, it is insufficient
76 alone to represent OA volatility. Direct volatility measurements, especially when paired with chemical composition
77 data, are necessary to improve our understanding of OA sources and aging processes.

78 In this study, we investigate the sources and volatility characteristics of OA in Seoul during winter. Wintertime OA
79 presents additional challenges due to its high complexity. During winter, emissions from combustion sources such
80 as biomass burning and residential heating significantly increase, contributing large amounts of primary OA (Kim
81 et al., 2017). Meanwhile, low ambient temperatures and reduced photochemical activity affect the formation and
82 evolution of secondary OA (SOA). Frequent haze events further complicate the aerosol properties by extending
83 aging times and increasing particle loadings. These overlapping sources and atmospheric conditions make winter
84 OA particularly difficult to characterize and predict. Despite Seoul's significance for air quality management,
85 comprehensive studies on OA volatility during winter remain limited. To address these goals, we conducted real-time,
86 high-resolution measurements using a high-resolution time-of-flight aerosol mass spectrometer (HR-ToF-AMS)
87 coupled with a thermodenuder (TD). The objectives of this study are to: (1) improve the understanding of

88 wintertime OA in Seoul, (2) characterize the volatility of OA associated with different sources, and (3) explore the
89 relationship between OA volatility and chemical composition.

90 **2 Experimental methods**

91 **2.1 Sampling Site and Measurement Period**

92 We conducted continuous real-time measurements in Seoul, South Korea, from 28 November to 28 December
93 2019. The sampling site was located in the northeastern part of the city (37.60° N, 127.05° E), approximately 7 km
94 from the city center, surrounded by major roadways and mixed commercial–residential land use. Air samples were
95 collected at an elevation of approximately 60 meters above sea level, on the fifth floor of a building. A detailed site
96 description has been reported previously for winter Seoul (Kim et al., 2017). During this period, the average
97 ambient temperature was $1.76 \pm 4.3^{\circ}$ C, and the average relative humidity (RH) was $56.9 \pm 17.5\%$, based on data
98 from the Korea Meteorological Administration (<http://www.kma.go.kr>).

99 **2.2 Instrumentation and Measurements**

100 The physico-chemical properties of non-refractory PM_1 (NR- PM_1) species—including sulfate, nitrate, ammonium,
101 chloride, and organics—were measured using an Aerodyne high-resolution time-of-flight aerosol mass
102 spectrometer (HR-ToF-AMS) (DeCarlo et al., 2006). PM_1 mass in this study is taken as NR- PM_1 (from AMS) +
103 black carbon (BC; measured by MAAP), which is appropriate for winter Seoul where refractory PM_1 (metal/sea-
104 salt/crustal) is minor and dust events were excluded (e.g., Kim et al., 2017; Nault et al., 2018; Kang et al., 2022;
105 Jeon et al., 2023). Data were acquired at 2.5-minute intervals, alternating between V and W modes. The V mode
106 provides higher sensitivity but lower resolution, suitable for mass quantification, whereas the W mode offers higher
107 mass resolution but lower sensitivity, used here for OA source apportionment. Simultaneously, black carbon (BC)
108 concentrations were measured at 1-minute intervals using a multi-angle absorption photometer (MAAP; Thermo
109 Fisher Scientific, Waltham, MA, USA). Total PM_1 mass was calculated as the sum of NR- PM_1 and BC.

110 Hourly trace gas concentrations (CO, O₃, NO₂, SO₂) were obtained from the Gireum air quality monitoring station
111 (37.61° N, 127.03° E), managed by the Seoul Research Institute of Public Health and Environment. Meteorological

112 data (temperature, RH, wind speed/direction) were collected from the nearby Jungreung site (37.61° N, 127.00°
113 E). All data are reported in Korea Standard Time (UTC+9).

114 To examine aerosol volatility, a thermodenuder (TD; Envalytix LLC) was installed upstream of the HR-ToF-AMS.
115 Details are provided in Supplementary Section S1 Kang et al. (2022). Briefly, ambient flow alternated every 5
116 minutes between a TD line and a bypass line at 1.1 L min^{-1} . Residence time in the TD line was $\sim 6.3 \text{ s}$. The TD
117 setup included a 50 cm heating section followed by an adsorption unit. Heated particles were stripped of volatile
118 species, while the downstream carbon-packed section prevented recondensation. TD temperature cycled through
119 12 steps (30 to 200 °C), with each step lasting 10 min (total cycle = 120 min). AMS V and W modes were alternated
120 during the same cycle. The heater was pre-adjusted to the next temperature while the bypass was active.

121

122 **2.3 Data Analysis**

123

124 **2.3.1 Data analysis and OA Source Apportionment**

125 HR-AMS data were processed using SQUIRREL v1.65B and PIKA v1.25B. Mass concentrations of non-refractory
126 PM₁ (NR-PM₁) species were derived from V-mode data, while high-resolution mass spectra (HRMS) and the
127 elemental composition of organic aerosols (OA) were obtained from W-mode data. NR-PM₁ quantification
128 followed established AMS protocols (Ulbrich et al., 2009; Zhang et al., 2011). Both the bypass and TD streams
129 were processed using a time-resolved, composition-dependent collection efficiency CE(t) following Middlebrook
130 et al. (2012). TD heating can modify particle water and phase state/mixing and thereby influence CE beyond
131 composition (Huffman et al., 2009), but prior TD-AMS studies indicate that such effects are modest and largely
132 multiplicative, which do not distort thermogram shapes or T₅₀ ordering (Faulhaber et al., 2009; Cappa & Jimenez,
133 2010). In our data, the CE(t) statistics for the two lines were similar (campaign-average CE: TD = 0.55 ± 0.08 ;
134 bypass = 0.53 ± 0.04 ; $\Delta = 0.02 \approx 3.7\%$, below the combined uncertainty ≈ 0.09). We therefore report volatility
135 metrics with these line-specific CE(t) corrections applied and interpret potential residual CE effects as minor. For
136 organics, elemental ratios (O:C, H:C, and OM/OC) were calculated using the Improved-Ambient (IA) method
137 (Canagaratna et al., 2015). Positive Matrix Factorization (PMF) was applied to the HRMS of organics using the
138 PMF2 algorithm (v4.2, robust mode) (Paatero and Tapper, 1994). The HRMS and corresponding error matrices
139 from PIKA were analyzed using the PMF Evaluation Tool v2.05 (Ulbrich et al., 2009). Data pretreatment followed
140 established protocols (Ulbrich et al., 2009; Zhang et al., 2011).

141 A six-factor solution (fPeak = 0; Q/Q_expected = 3.56) was selected as optimal (Fig. S1). The resolved OA sources
142 included hydrocarbon-like OA (HOA; 14%; O:C = 0.13), cooking-related OA (COA; 21%; O:C = 0.18), nitrogen-
143 enriched OA (NOA; 2%; O:C = 0.22), biomass-burning OA (BBOA; 13%; O:C = 0.25), less-oxidized oxygenated
144 OA (LO-OOA; 30%; O:C = 0.68), and more-oxidized oxygenated OA (MO-OOA; 20%; O:C = 1.15) (Figs. S2 and
145 S3). Alternative five- and seven-factor solutions were also evaluated. In the five-factor solution, the biomass
146 burning source was not clearly resolved and appeared to be distributed across multiple factors. In the seven-factor
147 solution, BBOA was further split into two separate factors without clear distinction or added interpretive value,
148 making the six-factor solution the most physically meaningful and interpretable (Figs. S4 and S5).

149

150 **2.3.2 Thermogram and Volatility Estimation**

151 The chemical composition dependent mass fraction remaining (MFR) was derived at each TD temperature by
152 dividing the corrected mass concentration of the TD line [p] by the average of the adjacent bypass lines [p-1] and
153 [p+1]. Thermograms were corrected for particle loss, estimated using reference substances like NaCl, which exhibit
154 minimal evaporation (Huffman et al., 2009; Saha et al., 2014; Kang et al., 2023). OA factor concentrations at each
155 TD temperature were derived via multivariate linear regression between post-TD HRMS and ambient OA factor
156 HRMS profiles as described in Zhou et al., 2016.

157 Volatility distributions were modeled using the thermodenuder mass transfer model from Riipinen et al. (2010) and
158 Karnezi et al. (2014), implemented in Igor Pro 9 (Kang et al., 2022). OA mass was distributed into eight logarithmic
159 saturation concentration bins (C^* : 1000 to $0.0001 \mu\text{g m}^{-3}$). Modeled MFRs were fit to observations using Igor's
160 "FuncFit" function, repeated 1,000 times per OA factor to determine best-fit results. The model assumes no thermal
161 decomposition and includes adjustable parameters: mass accommodation coefficient (α_m) and enthalpy of
162 vaporization (ΔH_{exp}), randomly sampled within literature-based ranges (Table S1).

163

164 **3 Results and discussion**

165 **3.1 Overview of PM₁ Composition and OA Sources**

166 We conducted continuous measurements from 28 November to 28 December 2019, characterizing a winter period
167 with a mean PM₁ concentration of $27.8 \pm 15.3 \mu\text{g m}^{-3}$. This concentration is characterized as moderate; it closely
168 matches historical winter PM₁ means in Seoul (Kim et al., 2017) and implies an equivalent PM_{2.5} concentration is
169 about $34.8 \mu\text{g m}^{-3}$ (using a Korea-specific PM₁/PM_{2.5} ≈ 0.8 (Kwon et al., 2023), which is near the national 24-h PM_{2.5}

170 standard ($35\mu\text{gm}^{-3}$) (AirKorea). The full co-evolution of PM_1 , gaseous pollutants, and meteorological conditions
171 is provided in Fig. S6, showing an average ambient temperature of $1.76\pm4.3^\circ\text{C}$ and average relative humidity (RH)
172 of $56.9\pm17.5\%$ during the study.

173 Figure 1 summarizes the overall non-refractory submicron aerosol (NR-PM1) composition and the identified OA
174 factors. Organics (41%) and nitrate (30%) were the most abundant chemical components of PM_1 , followed by
175 ammonium (12%), sulfate (10%), BC (5%), and chloride (3%) (Fig. 1a). Among the organic aerosols, six OA
176 factors were identified during the winter of 2019: hydrocarbon-like OA (HOA; 14%; O:C = 0.13), cooking-related
177 OA (COA; 21%; O:C = 0.18), nitrogen-enriched OA (NOA; 2%; O:C = 0.22), biomass burning OA (BBOA; 13%;
178 O:C = 0.25), and two types of secondary organic aerosols—less-oxidized oxygenated OA (LO-OOA; 30%; O:C =
179 0.68) and more-oxidized oxygenated OA (MO-OOA; 20%; O:C = 1.15) (Fig. 1e and Fig. S2). These compositions
180 are consistent with previous wintertime observations in Kim et al. (2017), with the exception of NOA, which will
181 be discussed in detail in Section 3.1.1.

182 PM_1 mass concentrations varied widely, ranging from 4.61 to $91.4\mu\text{g m}^{-3}$, largely due to two severe haze episodes
183 that occurred between December 7–12 and December 22–26 (Fig. 1). During these episodes, average
184 concentrations increased significantly, driven primarily by elevated levels of nitrate, MO-OOA, and NOA (Fig.
185 1f,g). Back-trajectory clustering shows frequent short-range recirculation over the Seoul Metropolitan Area during
186 haze (Cluster 1; Fig. S8), and the time series indicates persistently low surface wind speeds during these periods
187 (1.73 ± 0.89 vs. 2.34 ± 1.18 (clean)) (Fig. S6), together pointing to stagnation-driven accumulation of local emissions;
188 the concurrent increases in MO-OOA and NOA are therefore consistent with enhanced in-city formation under
189 stagnant conditions. Such haze episodes, characterized by local emission buildup and secondary aerosol production,
190 are a typical wintertime feature, as also reported in Kim et al. (2017).

191 **3.1.1 Nitrogen-containing organic aerosol (NOA)**

192 Unlike previous wintertime aerosol studies in Seoul, this study successfully resolved a nitrogen-containing organic
193 aerosol (NOA) factor by applying positive matrix factorization (PMF) to high-resolution AMS data. NOA
194 contributed approximately 2% of the total organic aerosol (OA) mass—comparable to urban observations in
195 Guangzhou (3%; Chen et al., 2021), Pasadena (5%; Hayes et al., 2013), and New York (5.8%; Sun et al., 2011).

196 Detection of particulate NOA using real time measurement has been challenging due to its low concentration and
197 high volatility. Although Baek et al. (2022) identified nitrogen-containing species in Seoul via year-round filter-

198 based molecular analysis, PMF-based resolution of NOA in real time has not been previously reported. The
199 successful identification in this study is likely attributable to favorable winter meteorological conditions—
200 specifically low temperatures (-0.24°C) and persistently high relative humidity ($\sim 57\%$) compared to the 2017
201 winter season (Kim et al., 2017)—that enhanced gas-to-particle partitioning of semi-volatile amines, thereby
202 enabling their detection (Fig. S2). NOA concentrations frequently exceeded $1 \mu\text{g m}^{-3}$ when RH surpassed 60% (Fig.
203 2), supporting the importance of RH-driven partitioning and the subsequent formation of low-volatility aminium
204 salts (Rovelli et al., 2017). Although extremely low temperatures may inhibit NOA formation due to the transition
205 of aerosol particles into solid phase (Ge et al., 2011; Srivastava et al., 2022), the combination of consistently cold
206 and humid conditions during the measurement period likely promoted the partitioning of semi-volatile amines into
207 the particle phase.

208 In addition, episodic haze events further elevated NOA levels, increasing its contribution to OA from 1% during
209 clean periods to as much as 3% (Fig. 1f–h). These high-concentration events likely improved the signal-to-noise
210 ratio, facilitating PMF resolution. Back-trajectory analysis linked these events to regional recirculation patterns
211 (Cluster 1, Fig. S7), suggesting a predominantly local origin—consistent with the short atmospheric lifetimes and
212 high reactivity of most amines (Ge et al., 2011; Nielsen et al., 2012; Hanson et al., 2014).

213 The NOA factor exhibited the highest nitrogen-to-carbon (N:C) ratio (0.22) and the lowest oxygen-to-carbon (O:C)
214 ratio (0.19) among all POA factors (Fig. S2), indicating a chemically reduced, nitrogen-rich composition. The
215 factor represents semi-volatile, reduced nitrogen species that originate from primary urban combustion sources but
216 whose observed mass in the particle phase is enhanced by rapid secondary partitioning and salt formation (Ge et
217 al., 2011; You et al., 2014). The NOA mass spectrum was dominated by amine-related fragments including m/z 30
218 (CH_4N^+), 44 ($\text{C}_2\text{H}_6\text{N}^+$), 58 ($\text{C}_3\text{H}_8\text{N}^+$), and 86 ($\text{C}_5\text{H}_{12}\text{N}^+$) (Fig. 3a). The spectral signature of the factor is defined by
219 the characteristic dominance of the m/z 44 fragment, which typically serves as the primary marker for
220 dimethylamine (DMA)-related species, closely followed by m/z 58 (trimethylamine, TMA) and m/z 30
221 (methylamine, MA). This profile is in strong agreement with NOA factors resolved via PMF in other polluted
222 environments. For instance, the dominance of m/z 44 and m/z 30 aligns with amine factors reported in New York
223 City (Sun et al., 2011) and Pasadena, California (Hayes et al., 2013). This DMA-dominated signature is also
224 consistent with seasonal characterization of organic nitrogen in Beijing (Xu et al., 2017) and Po Valley, Italy
225 (Saarikoski et al., 2012), reinforcing the common chemical signature of reduced organic nitrogen across diverse
226 urban and regional environments. Furthermore, the presence of non-negligible signals at m/z 58 and m/z 86 supports

227 the contribution of slightly larger alkylamines, a pattern that aligns well with established AMS laboratory reference
228 spectra for these reduced nitrogen compounds (Ge et al., 2011; Silva et al., 2008).

229 These amines are commonly emitted during the combustion of nitrogen-rich biomass and proteinaceous materials
230 and are frequently associated with biomass-burning emissions (Ge et al., 2011). Previous molecular analyses in
231 Seoul also indicate DMA, MA, and TMA as the dominant amine species in December (Baek et al., 2022). While
232 other amines such as triethylamine (TEA), diethylamine (DEA), and ethylamine (EA) may contribute via
233 industrial/solvent pathways (e.g., chemical manufacturing, petrochemical corridors, wastewater treatment), our
234 HR-AMS spectra are dominated by small alkylamine fragments (m/z 30, 44, 58, 86) and the diurnal behavior co-
235 varies with combustion markers (below), indicating a primarily combustion-linked influence. Nevertheless, recent
236 urban measurements and sector-based analyses show that industrial activities can contribute measurable amines in
237 cities (Tiszenkel et al., 2024; Zheng et al., 2015; Mao et al., 2018; Shen et al., 2017; Yao et al., 2016). Accordingly,
238 a minor NOA contribution from solvent/industrial amines cannot be excluded. Supporting this, NOA exhibited a
239 diurnal pattern similar to that of BBOA, with both peaking at night and in the early morning (Fig. 2a), suggesting
240 shared sources or formation mechanisms. Biomass burning under cold, oxygen-limited conditions is known to emit
241 various amines and amides (You et al., 2014; Yao et al., 2016), which may contribute directly to NOA or serve as
242 precursors for its secondary formation. Strong correlations with CH_4N^+ ($r = 0.95$) and $\text{C}_2\text{H}_6\text{N}^+$ ($r = 0.91$) (Fig. 2)
243 further support the presence of reduced nitrogen compounds, typically associated with residential fuel combustion
244 and wintertime heating. However, the time series of NOA and BBOA were not well correlated (Fig. 2 and S7),
245 likely because NOA episodes preferentially occurred during haze periods under stagnant conditions (Fig. 1),
246 whereas BBOA emissions tend to follow a more regular, daily emission pattern. Under cold, humid, and stagnant
247 conditions, these semi-volatile amines can readily partition into the particle phase and form low-volatility aminium
248 salts, enhancing the observed NOA signal. Taken together, these results suggest that NOA during wintertime in
249 Seoul is strongly influenced by a combination of combustion-related primary emissions and subsequent
250 atmospheric processing of amine-containing species, facilitated by seasonally favorable conditions.

251 **3.1.2 Secondary organic aerosols (SOA)**

252 In this study, two OOA factors—more-oxidized OOA (MO-OOA) and less-oxidized OOA (LO-OOA)—were
253 identified, together accounting for approximately half of the total organic aerosol (OA) mass. This fraction is
254 notably higher than that reported in previous wintertime urban studies (Kim et al., 2017; Zhang et al., 2007). Both
255 OOA exhibited characteristic mass spectral features, including prominent peaks at m/z 44 (CO_2^+) and m/z 43

256 ($\text{C}_2\text{H}_3\text{O}^+$), which are widely recognized as markers of oxygenated organics (Fig. S2e, S3f). The oxygen-to-carbon
257 (O:C) ratios for MO-OOA and LO-OOA were 1.15 and 0.68, respectively, indicating highly oxidized chemical
258 compositions. The O:C ratio of MO-OOA was especially elevated, exceeding those reported in previous Seoul
259 campaigns—0.68 in winter 2015 (Kim et al., 2017), 0.99 in spring 2019 (Kim et al., 2020), and 0.78 in fall 2019
260 (Jeon et al., 2023)—while the LO-OOA ratio was within a similar range.

261 MO-OOA showed strong correlations with secondary inorganic species such as nitrate ($r = 0.90$), ammonium ($r =$
262 0.92), and sulfate ($r = 0.81$), consistent with its formation through regional and local photochemical aging processes
263 (Fig. S3). In contrast, LO-OOA exhibited only modest correlations with sulfate, nitrate, and ammonium ($r = 0.50$,
264 0.51, and 0.42, respectively, suggesting additional contributions from semi-primary sources not closely linked to
265 inorganic secondary formation (e.g., cooking, traffic, biomass burning). LO-OOA does not exhibit a pronounced
266 m/z 60 (levoglucosan) signal (Fig. S2); however, the levoglucosan marker (f_{60}) is known to diminish with
267 atmospheric aging and can become weak or undetectable downwind (Hennigan et al., 2010; Cubison et al., 2011).
268 Taken together, the weaker coupling with secondary inorganics and the absence of a strong m/z 60 peak indicate
269 that LO-OOA is a mixture of aged secondary organics and semi-primary urban emissions, while a contribution
270 from aged biomass-burning influence cannot be ruled out..

271 **3.1.3 Primary organic aerosols (POA)**

272 Three primary organic aerosol (POA) factors were identified in this study: hydrocarbon-like OA (HOA), cooking-
273 related OA (COA), and biomass burning OA (BBOA). These three components exhibited mass spectral and
274 temporal characteristics consistent with previous observations in Seoul and other urban environments. HOA was
275 characterized by dominant alkyl fragment ions ($\text{C}_n\text{H}_{2n+1}^+$ and $\text{C}_n\text{H}_{2n-1}^+$; Fig. S2a) and a low O:C ratio (0.13),
276 consistent with traffic-related emissions (0.05–0.25) (Canagaratna et al., 2015). It showed strong correlations with
277 vehicle-related ions C_3H_7^+ ($r = 0.79$) and C_4H_9^+ ($r = 0.86$) (Kim et al., 2017; Canagaratna et al., 2004; Zhang et al.,
278 2005), and exhibited a distinct morning rush hour peak (06:00–08:00), followed by a decrease likely driven by
279 boundary layer expansion (Fig. S3a).

280 COA, accounting for 21% of OA, showed higher contributions from oxygenated ions than HOA, with tracer peaks
281 at m/z 55,84 and 98 (Fig. S2b) consistent with cooking emissions (Sun et al., 2011). It correlated strongly with

282 cooking-related ions such as $\text{C}_3\text{H}_3\text{O}^+$ ($r = 0.94$), $\text{C}_5\text{H}_8\text{O}^+$ ($r = 0.96$), and $\text{C}_6\text{H}_{10}\text{O}^+$ ($r = 0.98$) (Fig. S3h), and displayed
283 prominent peaks during lunch and dinner hours, reflecting typical cooking activity patterns.

284 BBOA was identified based on characteristic ions at m/z 60 ($\text{C}_2\text{H}_4\text{O}_2^+$) and 73 ($\text{C}_3\text{H}_5\text{O}^+$), both of which are
285 associated with levoglucosan—a well-established tracer for biomass burning (Simoneit et al., 2002). Its relatively
286 high f_{60} and low f_{44} values (Fig. S8a) indicate that the BBOA observed in this study was relatively fresh and had
287 not undergone extensive atmospheric aging (Cubison et al., 2011). Furthermore, BBOA exhibited moderate
288 correlations with NOA in both diurnal profiles and time series (Fig. 2), particularly with nitrogen-containing ions
289 such as $\text{C}_2\text{H}_4\text{N}^+$ ($r = 0.67$) and $\text{C}_2\text{H}_6\text{N}^+$ ($r = 0.56$) (Fig. 2 and S3), which are also dominant peaks in the NOA mass
290 spectrum. This overlap suggests a potential shared emission source or co-emission scenario, , consistent with the
291 co-emission of both organic aerosols and reduced nitrogen-containing compounds. Regarding source location,
292 several pathways can influence Seoul's biomass burning signature. First, urban/peri-urban small-scale burning
293 (e.g., solid-fuel use in select households, restaurant charcoal use, and intermittent waste burning) has been reported
294 and can enhance BBOA locally (Kim et al., 2017). Second, nearby agricultural-residue burning in surrounding
295 provinces occurs seasonally and can episodically impact the metropolitan area (Han et al., 2022). Third, regional
296 transport from upwind regions (e.g., northeastern China/North Korea) can bring biomass burning influenced air
297 masses under northerly/northwesterly flow (Lamb et al., 2018; Nault et al., 2018). In this dataset, the nighttime and
298 early-morning enhancements, the BBOA–NOA co-variation, and trajectory clusters showing regional recirculation
299 indicate a predominantly local/near-source contribution during the study period (Yoo et al., 2024), with episodic
300 non-local influences remaining possible.

301 **3.2 Volatility of Non-Refractory Species**

302 Figure 4 presents thermograms of non-refractory (NR) species measured by HR-ToF-AMS. The mass fraction
303 remaining (MFR) after thermodenuder (TD) treatment follows the typical volatility trend reported in previous
304 studies (Xu et al., 2016; Kang et al., 2022; Jeon et al., 2023; Huffman et al., 2009): nitrate was the most volatile,
305 followed by chloride, ammonium, organics, and sulfate. Nitrate showed the steepest decline with temperature, with
306 a T_{50} of ~ 67 °C—higher than pure ammonium nitrate (~ 37 °C; Huffman et al., 2009), suggesting contributions from
307 less volatile species like organonitrates or metal nitrates (Feng et al., 2023). Nearly complete evaporation occurred
308 by 200 °C ($\sim 2\%$ remaining). Compared to previously reported fall conditions ($T_{50} \sim 73$ °C, incomplete evaporation),
309 winter nitrate appeared more volatile, indicating relatively fewer non-volatile nitrate forms (e.g., Kang et al., 2022;
310 Jeon et al., 2023). Sulfate was the least volatile ($T_{50} \approx 170$ °C), consistent with ammonium sulfate (Scott and Cattell,

311 1979). A subtle slope change near 140 °C likely reflects ammonium-sulfate morphology/phase-state changes and/or
312 organosulfate–inorganic mixing, rather than contributions from metallic (refractory) sulfates, which are not
313 efficiently detected by AMS About 25% remained at 200 °C, indicating possible contributions from metallic or
314 organic sulfates. Ammonium showed intermediate volatility, with T_{50} between nitrate and sulfate. Its slightly lower
315 winter T_{50} suggests stronger nitrate association. Residual ammonium at 200 °C was consistent (~4%) in previously
316 reported spring/fall measurements (Kang et al., 2022; Jeon et al., 2023).. Chloride volatility was also comparable
317 across seasons in prior studies in terms of T_{50} , but exhibited more complete evaporation in winter (~4% residual
318 vs. ~10% in fall), possibly reflecting a shift in source to more volatile forms like road salt during wintertime..

319 OA exhibited moderate volatility (T_{50} ~120 °C), consistent with the presence of a wide variety of compounds with
320 differing volatilities. This trend aligns with previously reported spring and fall observations in Seoul, Korea (Kang et al.,
321 2022; Jeon et al., 2023).

322 3.2.1 Volatility Profiles of Organic sources

323 Figure 5 presents the volatility distributions of six OA sources within the volatility basis set (VBS) framework.
324 Volatility is expressed as the effective saturation concentration (C^* , $\mu\text{g m}^{-3}$), where higher C^* values correspond
325 to higher volatility. Following Donahue et al. (2009), C^* values are categorized into four bins: extremely low-
326 volatility organic compounds (ELVOCs, $\log C^* < -4.5$), low-volatility organic compounds (LVOCs, $-4.5 < \log$
327 $C^* < -0.5$), semi-volatile organic compounds (SVOCs, $-0.5 < \log C^* < 2.5$), and intermediate-volatility organic
328 compounds (IVOCs, $2.5 < \log C^* < 6.5$).

329 Among the primary OA (POA) sources, hydrocarbon-like OA (HOA) exhibited the highest volatility, with mass
330 predominantly distributed in the SVOC and IVOC ranges. This is consistent with its low oxidation state (O:C =
331 0.35) and primary emission characteristics. Mass fraction remaining (MFR) results (Fig. S9) further support this,
332 showing rapid mass loss at lower temperatures. Biomass burning OA (BBOA) and nitrogen-containing OA (NOA)
333 also showed high volatility, peaking in the SVOC–IVOC range ($\log C^* = 1–3$), and had lower O:C ratios of 0.25
334 and 0.19, respectively. Their slightly more oxidized nature relative to HOA, despite a similar volatility range, may
335 reflect emissions occurring under nighttime or cooler conditions, which promote condensation of otherwise volatile
336 species. The similar volatility distributions and MFR profiles of BBOA and NOA (Fig. S9) further support the
337 possibility of a shared emission source or formation pathway (Section 3.1.1). Cooking-related OA (COA) showed
338 a more moderate volatility profile, with mass more evenly distributed across the LVOC and SVOC bins. This

339 pattern reflects its diverse cooking sources and variable emission profiles as previously reported (Kang et al.,
340 2022)..

341 For secondary OA (SOA), less-oxidized oxygenated OA (LO-OOA) exhibited the lowest volatility, with substantial
342 mass in the LVOC and ELVOC bins ($C^* \approx 10^{-3}\text{--}10^{-4}$). This is in agreement with previous findings in Seoul during
343 spring (Kang et al., 2022). In contrast, more-oxidized OOA (MO-OOA), despite its higher oxidation state (O:C =
344 1.15), displayed greater volatility, with a peak at $C^* \approx 10^1$. This discrepancy likely reflects differences in formation
345 and aging processes, as discussed further in Section 3.3.

346 Overall, the volatility characteristics across OA factors suggest that oxidation state alone does not fully explain
347 volatility. Rather, volatility is shaped by a combination of emission source, emission timing, temperature, and
348 atmospheric processing. These findings highlight the importance of integrating both chemical and physical
349 characterization to better understand OA formation and aging across seasons.

350 **3.3 Aging effect on volatility from 2D VBS**

351 Generally, the oxygen-to-carbon (O:C) ratio of organic aerosols (OA) is inversely related to their volatility. As O:C
352 increases through aging, the effective saturation concentration (C^*) typically decreases, resulting in lower volatility
353 (Donahue et al., 2006; Jimenez et al., 2009). This common relationship arises because the addition of oxygen-
354 containing functional groups (e.g., hydroxyl, carboxyl, carbonyl), which increases molecular weight and enhances
355 intermolecular interactions such as hydrogen bonding, thereby reducing vapor pressure (Jimenez et al., 2009; Kroll
356 and Seinfeld, 2008). Moreover, oxidative aging often leads to oligomerization or functionalization, promoting
357 particle-phase retention and reducing the effective saturation concentration (C^*) (Donahue et al., 2011; Robinson
358 et al., 2007). However, in this study, the most oxidized OA factor—MO-OOA, with a high O:C ratio of 1.15—
359 exhibited unexpectedly high volatility. Its volatility distribution was skewed toward SVOCs and IVOCs (Fig. 5),
360 and its rapid mass loss in MFR thermograms (Fig. S9) further indicated low thermal stability. This observation
361 appears to contradict the usual inverse O:C–volatility relationship; however, under winter haze conditions—with
362 suppressed O_3 /low OH, particle-phase autoxidation and fragmentation can yield higher-O:C yet more volatile
363 products, with enhanced condensation on abundant particle surface area (details below).

364 Viewed against prior TD-AMS results, the volatility of Seoul's winter MO-OOA presents a unique case,
365 particularly in the nature of its O:C-volatility relationship. Prior urban studies have commonly reported substantial
366 SVOC-OA, consistent with high photochemical activity or elevated loadings; for example, Mexico City/Los

367 Angeles showed pronounced SVOC–IVOC contributions during warm seasons (Cappa and Jimenez, 2010), and
368 summertime Beijing and wintertime Shenzhen likewise exhibited strong overall OA volatility (Xu et al., 2019; Cao
369 et al., 2018). While these comparisons establish that volatile OA is common, they generally did not report the
370 factor-level inversion observed here, where the highly-oxidized OOA component (MO-OOA) was more volatile
371 than a less-oxidized OOA (LO-OOA). This behavior is distinct from findings in colder, lower-loading regimes;
372 wintertime Paris, for instance, maintained the conventional hierarchy where the more-oxidized OOA was
373 comparatively less volatile (Paciga et al., 2016). Furthermore, seasonal context within Seoul showed springtime
374 OA with lower oxidation levels than our winter MO-OOA despite similar SVOC contributions (Kang et al., 2022).
375 This comprehensive comparison underscores the unusual nature of the O:C-volatility relationship observed under
376 the specific winter haze conditions in Seoul.

377

378 3.3.1 Proposed Mechanism: Fragmentation and Condensation under Low-OH Haze

379 MO-OOA concentrations increased during haze episodes—characterized by reduced ozone levels, low solar
380 radiation and elevated aerosol mass concentrations (Fig. 6 and Fig. S6, yellow shading). The suppressed ozone
381 likely indicates lower OH radical production via O_3 photolysis, leading to a low-OH oxidation regime. We note
382 that haze also suppresses HONO photolysis; however, HONO concentrations can be elevated at night and early
383 morning via heterogeneous NO_2 conversion and surface emissions, so net OH from HONO may remain non-
384 negligible even as photolysis rates are depressed (e.g., Gil et al., 2021; Kim et al., 2024; Slater et al., 2020). Under
385 such conditions, particle-phase autoxidation involving RO_2 radicals can become the dominant oxidation pathway.
386 Even under low-OH conditions, NO_3 formed via $NO_2 + O_3$ can initiate RO_2 production through addition to alkenes,
387 while reduced photolysis at night/low light extends NO_3 lifetimes; these RO_2 then participate in particle-phase
388 autoxidation, yielding highly oxygenated yet relatively volatile products. These processes tend to produce highly
389 oxidized but relatively low-molecular-weight products (Ehn et al., 2014; Zhao et al., 2023). Unlike classical OH-
390 initiated, multi-generational aging—which increases molecular mass and reduces volatility—fragmentation-
391 dominated oxidation can cleave larger precursors into smaller oxygenated compounds, resulting in higher volatility
392 despite elevated O:C. Consistent with this interpretation, online AMS/FIGAERO-CIMS and EESI-TOF, as well as
393 offline HRMS/GC-MS, have reported high-O:C yet more-volatile product distributions accompanied by elevated f_{44}
394 with comparatively stable f_{43} under fragmentation-dominated aging (Kroll et al., 2009; Ng et al., 2010; Chhabra et
395 al., 2011; Lambe et al., 2012; Lopez-Hilfiker et al., 2016; D’Ambro et al., 2017). Furthermore, high aerosol mass
396 loadings during haze events provide abundant surface area for the uptake of semi-volatile/intermediate-volatility

397 organics via absorptive partitioning, so that higher C_{OA} enhances condensation (Pankow, 1994; Donahue et al.,
398 2006; Hallquist et al., 2009; Robinson et al., 2007). We also note that functionalized, low-molecular-weight
399 compounds can reside in the SVOC–IVOC range and thus contribute to the high apparent volatility of MO-OOA
400 (Ng et al., 2010; Chhabra et al., 2011; Lopez-Hilfiker et al., 2016; D’Ambro et al., 2017). . This facilitates the
401 condensation of even relatively volatile, oxidized compounds onto particles (Fig. 6). The net result is an apparent
402 increase in both oxidation state and volatility of OA, as reported in aging studies under stagnant and polluted
403 conditions (Jimenez et al., 2009; Ng et al., 2016).

404 In line with these reports, our results also revealed a decoupling between O:C and volatility, with MO-OOA
405 showing high volatility despite its elevated O:C ratio (~1.15). While this behavior has been observed in other urban
406 environments, this study provides one of the first detailed thermodynamic assessments of this decoupling under
407 winter haze conditions in Seoul using real-time TD-AMS measurements. Supporting this interpretation, MO-OOA
408 in this study was characterized by a consistently high f_{44} (CO_2^+) signal and a relatively stable f_{43} ($C_2H_3O^+$) signal
409 compared to LO-OOA (Fig. S8b). During specific periods when MO-OOA concentrations increased, only f_{44} was
410 noticeably enhanced, while f_{43} remained flat (Fig. 6). This temporal pattern—elevated f_{44} without corresponding
411 changes in f_{43} —is a typical signature of highly oxidized and fragmented organic aerosol and suggests advanced
412 aging dominated by fragmentation rather than functionalization (Kroll et al., 2009). Consistent with this, the haze–
413 non-haze comparison, including the high-MO-OOA interval (Fig. S12), shows larger oxygenated fragments (m/z 28, 29, 44)
414 and higher f_{44} and O:C during haze, whereas non-haze periods exhibit relatively larger fractional hydrocarbon fragments (m/z
415 41, 43, 55, 57). These spectral contrasts indicate that the elevated volatility of MO-OOA reflects advanced oxidation—via
416 autoxidation and the condensation of small oxygenated fragments—rather than enrichment of high-molecular-weight ions,
417 particularly under conditions of limited OH and high particulate surface area.

418 This unexpected volatility behavior of highly oxidized MO-OOA highlights the need for secondary organic aerosol
419 (SOA) models to incorporate fragmentation-dominated oxidation pathways—especially under haze conditions
420 where conventional assumptions linking O:C to volatility may break down. Including such mechanisms could
421 improve model accuracy in representing OA aging and volatility in urban air quality simulations.

422 **4 Conclusions**

423 This study offers a detailed characterization of wintertime submicron aerosols (PM_1) in Seoul by integrating
424 chemical composition, volatility behavior, and source apportionment to better understand their formation and

425 atmospheric evolution. Organic aerosols (OA), particularly secondary organic aerosols (SOA), were the dominant
426 PM₁ component, highlighting the significance of oxidative processes even during cold seasons. A notable result is
427 the successful real-time resolution of a nitrogen-containing organic aerosol (NOA) factor, enabled by cold, humid
428 meteorological conditions that enhanced the partitioning and stabilization of amine-derived compounds. The NOA
429 factor was characterized by tracer ions associated with low-molecular-weight alkylamines such as TMA, DMA,
430 and MA, which likely originated from biomass combustion.

431

432 Volatility analysis revealed distinct thermodynamic behavior across OA sources. Primary OA factors such as HOA,
433 BBOA, and COA exhibited relatively high volatility, while LO-OOA showed low volatility and a higher oxidation
434 state, consistent with aged, low-volatility material. The similarity in volatility distributions and diurnal patterns
435 between BBOA and NOA suggests that biomass combustion under wintertime conditions is a likely contributor to
436 both primary organic and nitrogenous aerosol formation.

437

438 Interestingly, MO-OOA—despite its high oxygen-to-carbon (O:C) ratio—exhibited elevated volatility, diverging
439 from the expected inverse relationship between oxidation state and volatility. This suggests that under stagnant,
440 polluted conditions with suppressed ozone and OH radical levels, particle-phase autoxidation and fragmentation
441 pathways may dominate over traditional OH-initiated aging, yielding highly oxidized yet semi-volatile products.
442 These findings highlight the importance of coupling high-resolution chemical and physical aerosol measurements
443 to better understand OA formation processes and properties within urban air quality frameworks. Consequently,
444 air quality models should incorporate diverse oxidation mechanisms and avoid assuming a direct link between
445 oxidation state and volatility.

446 **Data availability.**

447 Data presented in this article are available upon request to the corresponding author.

448 **Acknowledgements**

449 This work was supported by the National Research Foundation of Korea (NRF) grant funded by the Korea government (MSIT)
450 (RS-2025-00514570), the project “development of SMaRT based aerosol measurement and analysis systems for the evaluation
451 of climate change and health risk assessment” operated by Seoul National University (900-20240101).

452 **Author Contributions**

453 Hwajin Kim designed and prepared the manuscript. Jiwoo Jeong operated the TD-AMS and analyse the data. Jihye Moon
454 analyse the data. Hyungu Kang analyse the volatility of OA.

455

456 **Competing interests.**

457 The authors declare that they have no conflict of interest.

458

459

460

461

462

463

464

465

466

467

468

469

470

471

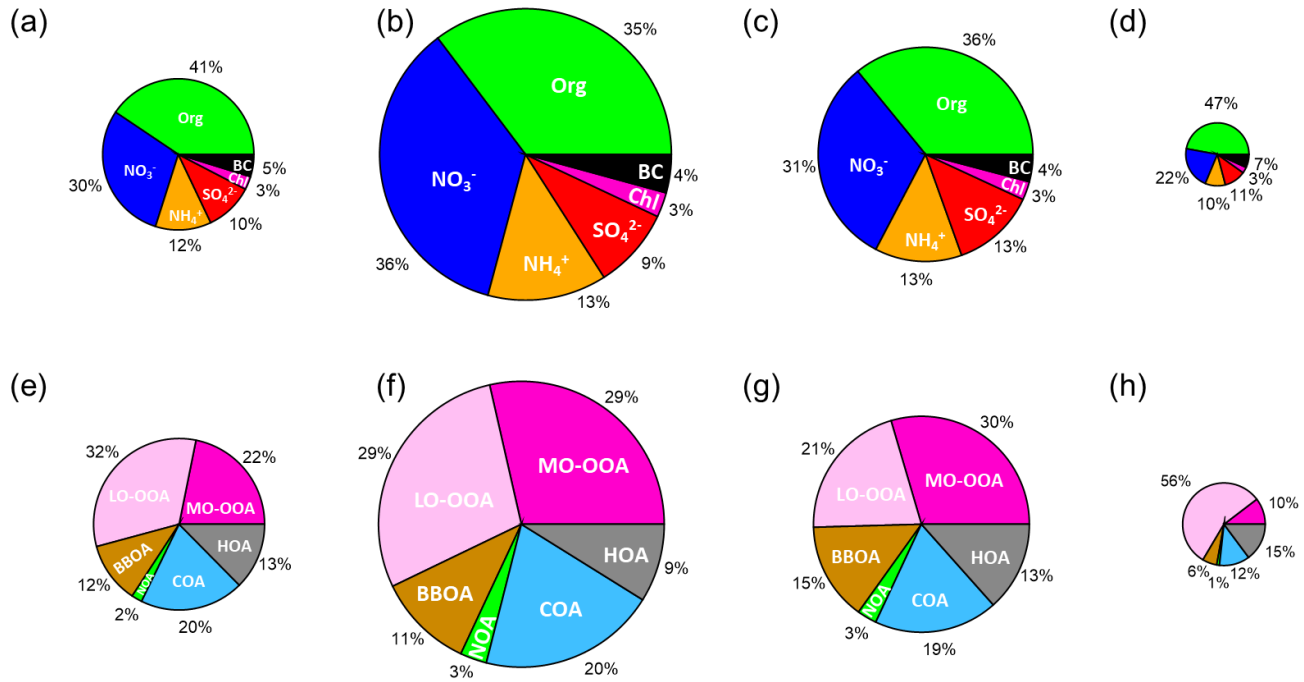
472

473

474

475

476
477
478 **Tables and Figures**
479
480
481



482
483
484
485
486
487

| Period | Standard | Avg. Mass conc. ($\mu\text{g m}^{-3}$) |
|---------------|-------------------------|------------------------------------------|
| Total | 2019.11.28 ~ 2019.12.28 | Avg $\text{PM}_1 = 26.37$ |
| Clean | 2019.12.04 ~ 2019.12.06 | Avg $\text{PM}_1 = 9.98$ |
| Haze 1 | 2019.12.07 ~ 2019.12.11 | Avg $\text{PM}_1 = 51.88$ |
| Haze 2 | 2019.12.21 ~ 2019.12.25 | Avg $\text{PM}_1 = 37.71$ |

Figure 1. Compositional pie charts of PM_1 species for (a) the entire study period, (b) haze period 1, (c) haze period 2, and (d) a clean period; and of each OA source for (e) the entire study period, (f) haze period 1, (g) haze period 2, and (h) the clean period. Table. Standard and average PM_1 mass concentrations during the entire study period, haze period 1, haze period 2, and the clean period.

488
489
490
491
492
493
494

495
496
497
498

499

500

501
502
503

504
505
506

507

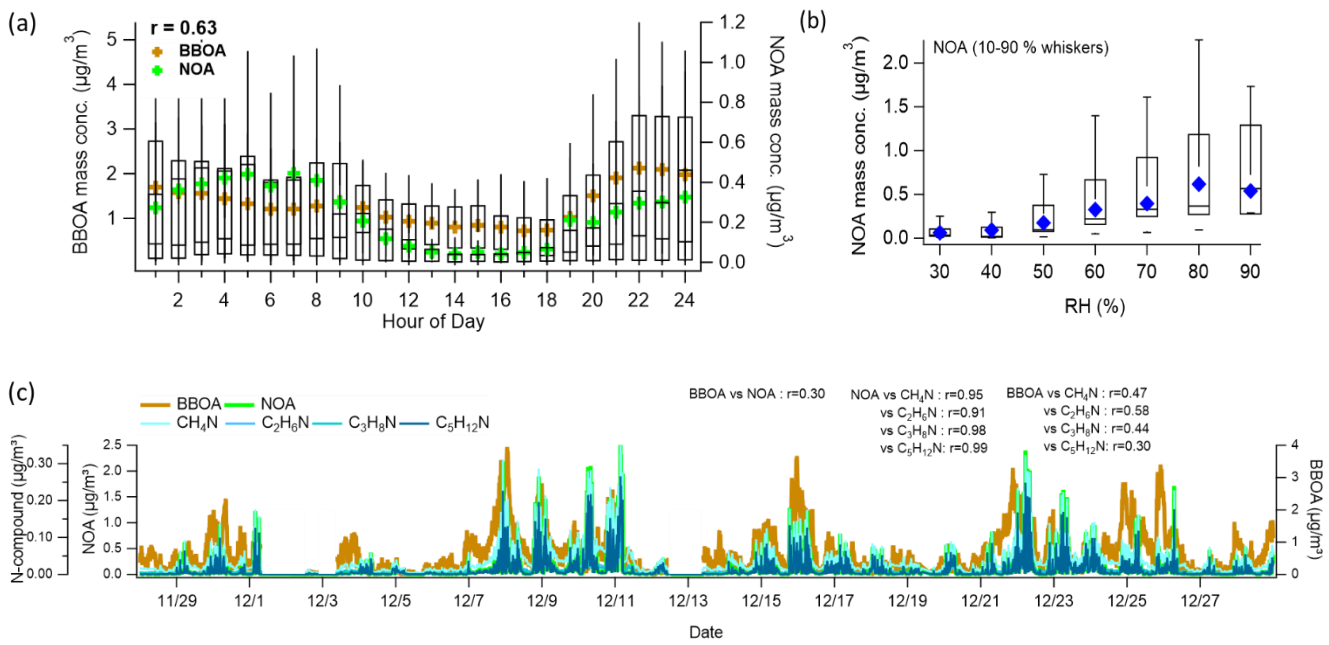
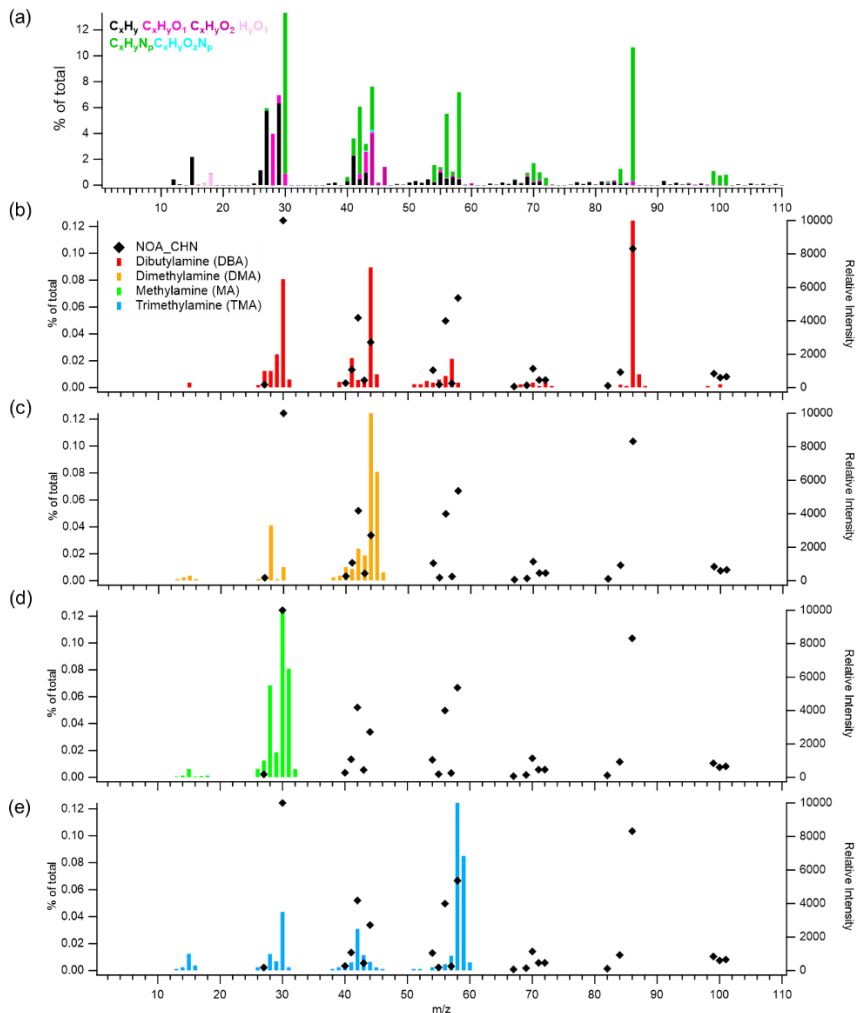
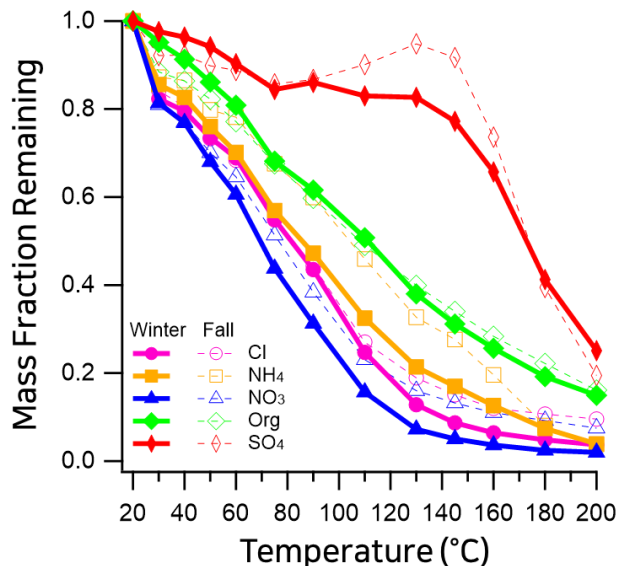


Figure 2. (a) Diurnal mean profiles of NOA and BBOA. Whiskers denote the 90th and 10th percentiles; box edges represent the 75th and 25th percentiles; the horizontal line indicates the median, and the colored marker shows the mean. The diurnal correlation between NOA and BBOA mean values is 0.63. (b) Relative humidity (RH)-binned nighttime (19:00–05:00) profile of NOA. Box and whisker definitions are the same as in panel (a). (c) Time series of NOA, BBOA, and amine-related ions (CH_4N^+ , $\text{C}_2\text{H}_6\text{N}^+$, $\text{C}_3\text{H}_8\text{N}^+$, $\text{C}_5\text{H}_{12}\text{N}^+$), along with their correlations with NOA and BBOA.

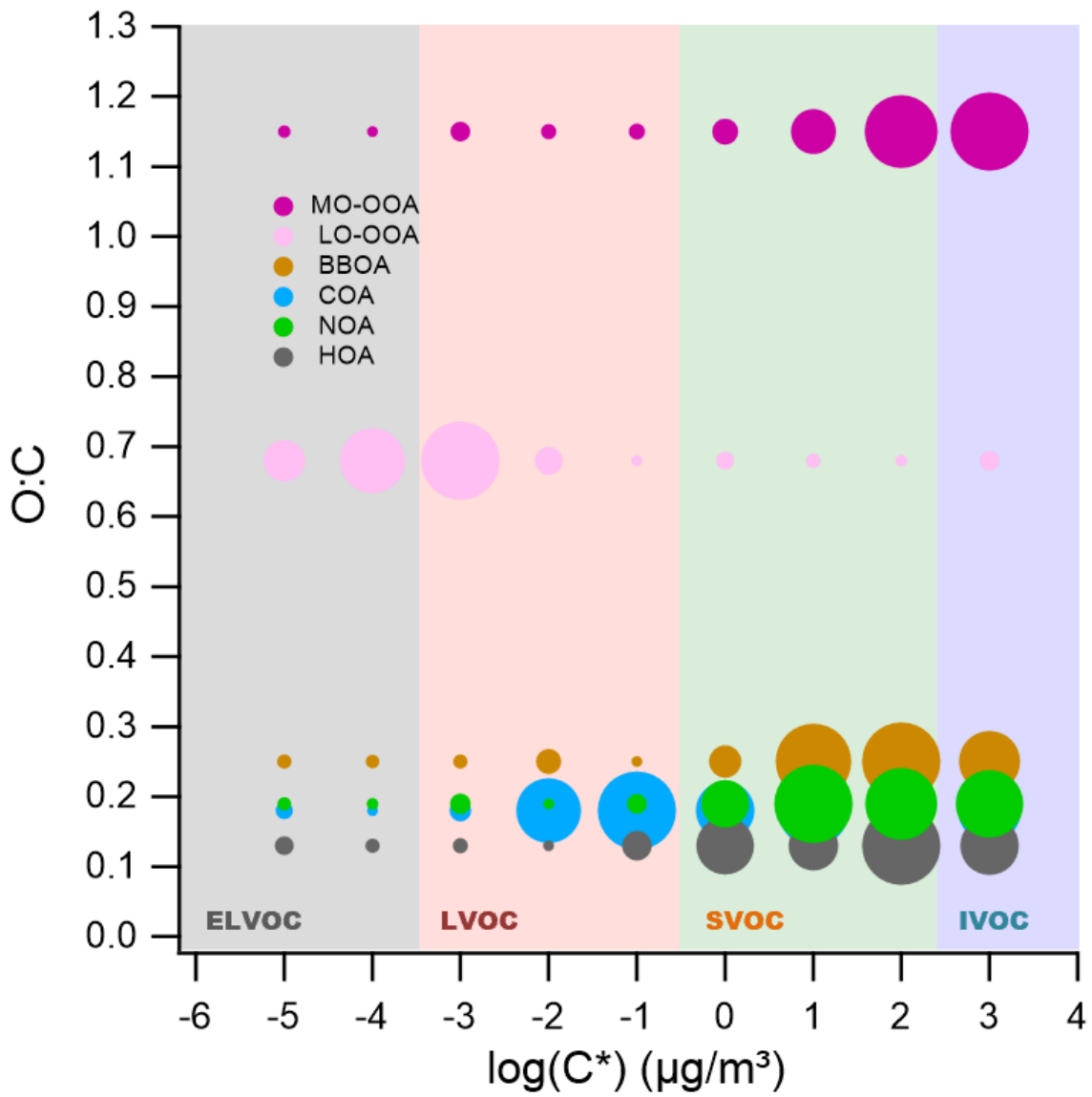


508
509
510
511
512
513
514
515

Figure 3. Mass spectra of (a) the NOA factor resolved by PMF analysis in this study, and reference spectra of amines from the NIST library: (b) dibutylamine (DBA), (c) dimethylamine (DMA), (d) methylamine (MA), and (e) trimethylamine (TMA). In panels (b)–(e), the left y-axis indicates the contribution of CHN-containing ions in the NOA factor (% of total), while the right y-axis shows the relative intensity of each compound's mass spectrum from the NIST library.

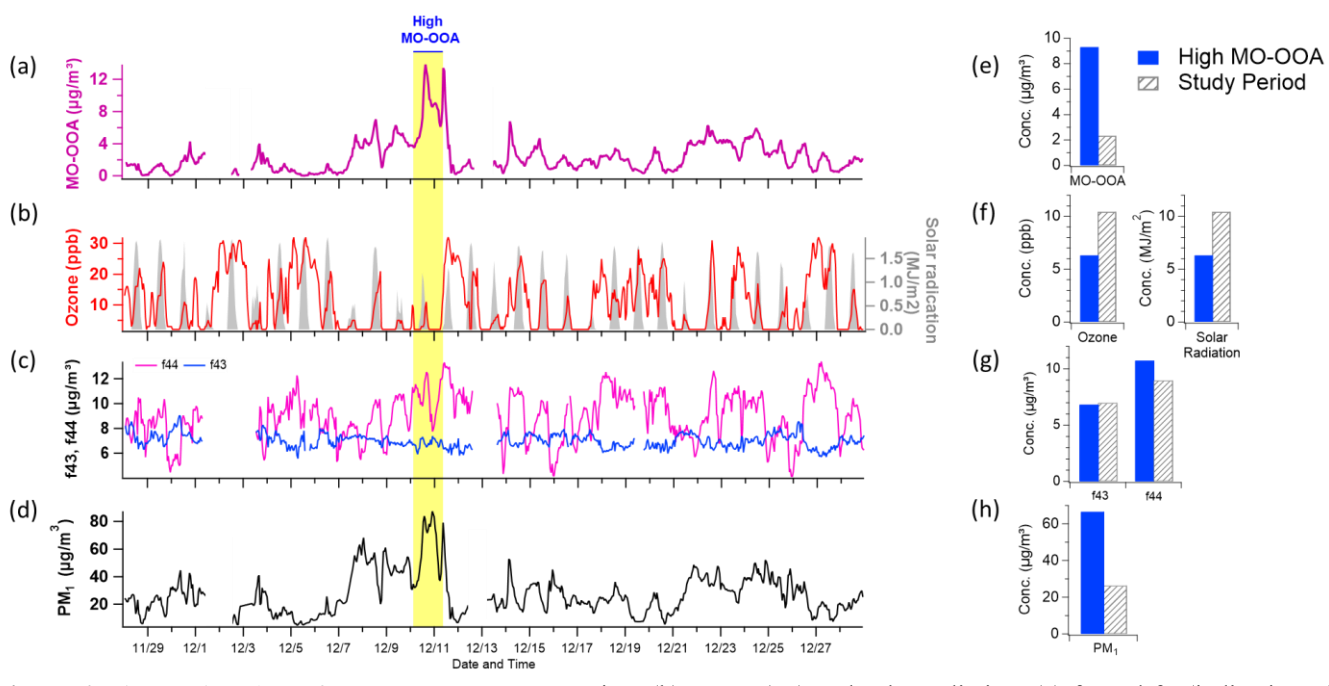


516 **Figure 4.** Mass fraction remaining (MFR) of non-refractory (NR) aerosol species measured in Seoul using a thermodenuder
 517 coupled to a high-resolution time-of-flight aerosol mass spectrometer (HR-ToF-AMS). Winter 2019 (this study; dashed) is
 518 compared with fall 2019 (previously reported; solid) (Jeon et al., 2023). Species include organics (magenta), nitrate (blue),
 519 sulfate (orange), ammonium (green), and chloride (red).



520
 521
Figure 5. Two-dimensional volatility basis set (2D-VBS) representation of organic aerosol (OA) sources identified in winter
 522 2019 in Seoul. The plot illustrates the relationship between the oxygen-to-carbon (O:C) ratio and the effective saturation
 523 concentration (C^*) for each OA source resolved via positive matrix factorization (PMF). Solid circles represent the volatility
 524 distribution across C^* bins, with marker size proportional to the mass fraction within each bin for the given source. Shaded
 525 regions correspond to different volatility classes: extremely low-volatility organic compounds (ELVOCs), low-volatility
 526 organic compounds (LVOCs), semi-volatile organic compounds (SVOCs), and intermediate-volatility organic compounds
 527 (IVOCs), delineated by their C^* values.
 528
 529
 530
 531

532
533
534
535
536
537
538
539
540
541
542
543
544
545
546
547
548



549
550 **Figure 6.** Time series plots of (a) MO-OOA concentration, (b) ozone (O_3) and solar radiation, (c) f_{44} and f_{43} (indicative of
551 oxidation state), and (d) total PM_1 concentration. The period characterized by elevated MO-OOA levels is highlighted in bright
552 yellow. Panels (e)–(f) present comparative distributions of these variables—MO-OOA, O_3 and solar radiation, f_{44} and f_{43} , and
553 PM_1 —between the high MO-OOA period (shaded in blue) and the entire measurement period (indicated by gray hatching).

554
555
556
557
558

559 **References**

560 Ghim, Y. S., Moon, K.-C., Lee, S., Kim, Y. P., 2005. Visibility trends in Korea during the past two decades. *J. Air Waste*
561 *Manag. Assoc.* 55, 73–82. <https://doi.org/10.1080/10473289.2005.10464599>

562 Zhao, H., Che, H., Zhang, X., Ma, Y., Wang, Y., Wang, H., Wang, Y., 2013. Characteristics of visibility and particulate matter
563 (PM) in an urban area of Northeast China. *Atmos. Pollut. Res.* 4, 427–434. <https://doi.org/10.5094/APR.2013.049>

564 Hamanaka, R. B., Mutlu, G. M., 2018. Particulate matter air pollution: Effects on the cardiovascular system. *Front. Endocrinol.*
565 9, 680. <https://doi.org/10.3389/fendo.2018.00680>

566 Manisalidis, I., Stavropoulou, E., Starvropoulos, A., Bezirtzoglou, E., 2020. Environmental and health impacts of air pollution:
567 a review. *Front. Public Health* 8, 14. <https://doi.org/10.3389/fpubh.2020.00014>

568 IPCC, 2021. Climate Change 2021: The Physical Science Basis. Contribution of Working Group I to the Sixth Assessment
569 Report of the Intergovernmental Panel on Climate Change, edited by Masson-Delmotte, V., Zhai, P., Pirani, A., Connors,
570 S.L., Péan, C., Berger, S., et al. Cambridge University Press, Cambridge, UK and New York, NY, USA, pp. 817–922.
571 <https://doi.org/10.1017/9781009157896.008>

572 Zhang, Q., Jimenez, J. L., Canagaratna, M. R., Allan, J. D., Coe, H., Ulbrich, I., Alfarra, M. R., Takami, A., Middlebrook, A.
573 M., Sun, Y. L., Dzepina, K., Dunlea, E., Docherty, K., DeCarlo, P., Salcedo, D., Onasch, T. B., Jayne, J. T., Miyoshi, T.,
574 Shimono, A., Hatakeyama, N., Takegawa, N., Kondo, Y., Schneider, J., Drewnick, F., Weimer, S., Demerjian, K. L.,
575 Williams, P. I., Bower, K. N., Bahreini, R., Cottrell, L., Griffin, R. J., Rautianen, J., Worsnop, D. R., 2007. Ubiquity and
576 dominance of oxygenated species in organic aerosols in anthropogenically-influenced Northern Hemisphere mid-latitudes.
577 *Geophys. Res. Lett.* 34, L13801. <https://doi.org/10.1029/2007GL029979>

578 Jimenez, J. L., Canagaratna, M. R., Donahue, N. M., Prevot, A. S. H., Zhang, Q., Kroll, J. H., ... Worsnop, D. R., 2009.
579 Evolution of organic aerosols in the atmosphere. *Science* 326, 1525–1529. <https://doi.org/10.1126/science.1180353>

580 Hallquist, M., Wenger, J. C., Baltensperger, U., Rudich, Y., Simpson, D., Claeys, M., ... Seinfeld, J. H., 2009. The formation,
581 properties and impact of secondary organic aerosol: current and emerging issues. *Atmos. Chem. Phys.* 9, 5155–5236.
582 <https://doi.org/10.5194/acp-9-5155-2009>

583 Robinson, A. L., Donahue, N. M., Shrivastava, M. K., Weitkamp, E. A., Sage, A. M., Grieshop, A. P., Lane, T. E., Pierce, J.
584 R., Pandis, S. N., 2007. Rethinking organic aerosols: Semivolatile emissions and photochemical aging. *Science* 315, 1259–
585 1262. <https://doi.org/10.1126/science.1133061>

586 Donahue, N. M., Robinson, A. L., Stanier, C. O., Pandis, S. N., 2006. Coupled partitioning, dilution, and chemical aging of
587 semivolatile organics. *Environ. Sci. Technol.* 40, 2635–2643. <https://doi.org/10.1021/es052297c>

588 Ng, N. L., Canagaratna, M. R., Zhang, Q., Jimenez, J. L., Tian, J., Ulbrich, I. M., Kroll, J. H., Docherty, K. S., Chhabra, P. S.,
589 Bahreini, R., Murphy, S. M., Seinfeld, J. H., Hildebrandt, L., Donahue, N. M., DeCarlo, P. F., Lanz, V. A., Prévôt, A. S.
590 H., Dinar, E., Rudich, Y., Worsnop, D. R., 2010. Organic aerosol components observed in Northern Hemispheric datasets
591 from Aerosol Mass Spectrometry. *Atmos. Chem. Phys.* 10, 4625–4641. <https://doi.org/10.5194/acp-10-4625-2010>

592 Cappa, C. D., Jimenez, J. L., 2010. Quantitative estimates of the volatility of ambient organic aerosol. *Atmos. Chem. Phys.*
593 10, 5409–5424. <https://doi.org/10.5194/acp-10-5409-2010>

594 Sinha, A., George, I., Holder, A., Preston, W., Hays, M., Grieshop, A. P., 2023. Development of volatility distributions for
595 organic matter in biomass burning emissions. *Environ. Sci. Adv.* 3, 11–23. <https://doi.org/10.1039/D2EA00080F>

596 Glasius, M., Goldstein, A. H., 2016. Recent discoveries and future challenges in atmospheric organic chemistry. *Environ. Sci.*
597 *Technol.* 50, 2754–2764. <https://doi.org/10.1021/acs.est.5b05105>

598 Matsui, H., Koike, M., Takegawa, N., Kondo, Y., Griffin, R. J., Miyazaki, Y., Yokouchi, Y., Ohara, T., 2009. Secondary
599 organic aerosol formation in urban air: Temporal variations and possible contributions from unidentified hydrocarbons. *J.*
600 *Geophys. Res. Atmos.* 114, D02209. <https://doi.org/10.1029/2008JD010164>

601 Jiang, F., Liu, Q., Huang, X., Wang, T., Zhuang, B., Xie, M., 2012. Regional modelling of secondary organic aerosol over
602 China using WRF/Chem. *J. Aerosol Sci.* 53, 50–61. <https://doi.org/10.1016/j.jaerosci.2011.09.003>

603 Li, J., Zhang, M., Wu, F., Sun, Y., Tang, G., 2017. Assessment of the impacts of aromatic VOC emissions and yields of SOA
604 on SOA concentrations with the air quality model RAMS-CMAQ. *Atmos. Environ.* 158, 105–115.
605 <https://doi.org/10.1016/j.atmosenv.2017.03.035>

606 Zhao, B., Wang, S., Donahue, N. M., Jathar, S. H., Huang, X., Wu, W., ... & Hao, J. (2016). Quantifying the effect of organic
607 aerosol aging and intermediate-volatility emissions on regional-scale aerosol pollution in China. *Scientific Reports*, 6,
608 28815. <https://doi.org/10.1038/srep28815>

609 Kang, H. G., Kim, Y., Collier, S., Zhang, Q., Kim, H., 2022. Volatility of springtime ambient organic aerosol derived with
610 thermodenuder aerosol mass spectrometry in Seoul, Korea. *Environ. Pollut.* 310, 119203.
611 <https://doi.org/10.1016/j.envpol.2022.119203>

612 Huang, X.-F., He, L.-Y., Hu, M., Canagaratna, M. R., Sun, Y., Zhang, Q., Worsnop, D. R., 2010. Highly time-resolved
613 chemical characterization of atmospheric submicron particles during 2008 Beijing Olympic Games using an Aerodyne
614 High-Resolution Aerosol Mass Spectrometer. *Atmos. Chem. Phys.* 10, 8933–8945. <https://doi.org/10.5194/acp-10-8933-2010>

615 Mohr, C., DeCarlo, P. F., Heringa, M. F., Chirico, R., Slowik, J. G., Richter, R., Reche, C., Alastuey, A., Querol, X., Seco, R.,
616 Peñuelas, J., Jiménez, J. L., Crippa, M., Zimmermann, R., Baltensperger, U., Prévôt, A. S. H., 2012. Identification and
617 quantification of organic aerosol from cooking and other sources in Barcelona using aerosol mass spectrometer data.
618 *Atmos. Chem. Phys.* 12, 1649–1665. <https://doi.org/10.5194/acp-12-1649-2012>

619 Xu, L., Kollman, M. S., Song, C., Shilling, J. E., Ng, N. L., 2014. Effects of NO_x on the volatility of secondary organic aerosol
620 from isoprene photooxidation. *Environ. Sci. Technol.* 48, 2253–2262. <https://doi.org/10.1021/es404842g>

621 Grieshop, A. P., Logue, J. M., Donahue, N. M., Robinson, A. L., 2009. Laboratory investigation of photochemical oxidation
622 of organic aerosol from wood fires 1: Measurement and simulation of organic aerosol evolution. *Atmos. Chem. Phys.* 9,
623 1263–1277. <https://doi.org/10.5194/acp-9-1263-2009>

625 Kim, H., Zhang, Q., Bae, G.-N., Kim, J.Y., Lee, S.B., 2017. Sources and atmospheric processing of winter aerosols in Seoul,
626 Korea: Insights from real-time measurements using a high-resolution aerosol mass spectrometer. *Atmos. Chem. Phys.* 17,
627 2009–2033. <https://doi.org/10.5194/acp-17-2009-2017>

628 DeCarlo, P. F., Kimmel, J. R., Trimborn, A., Northway, M. J., Jayne, A. E., Aiken, A. C., ... & Jimenez, J. L. (2006). Field-
629 deployable, high-resolution, time-of-flight aerosol mass spectrometer. *Analytical Chemistry*, 78(24), 8281–8289.
630 <https://doi.org/10.1021/ac061249>

631 Canagaratna, M. R., Jimenez, J. L., Kroll, J. H., Chen, Q., Kessler, S. H., Massoli, P., ... & Worsnop, D. R. (2015). Elemental
632 ratio measurements of organic compounds using aerosol mass spectrometry: Improved sensitivity and intercomparability.
633 *Atmospheric Chemistry and Physics*, 15(1), 253–272. <https://doi.org/10.5194/acp-15-253-2015>

634 Paatero, P., Tapper, U., 1994. Positive matrix factorization – A nonnegative factor model with optimal utilization of error
635 estimates of data values. *Environmetrics* 5, 111–126. <https://doi.org/10.1002/env.3170050203>

636 Ulbrich, I. M., Canagaratna, M. R., Zhang, Q., Worsnop, D. R., Jimenez, J. L., 2009. Interpretation of organic components
637 from Positive Matrix Factorization of aerosol mass spectrometric data. *Atmos. Chem. Phys.* 9, 2891–2918.
638 <https://doi.org/10.5194/acp-9-2891-2009>

639 Zhang, Q., Jimenez, J. L., Canagaratna, M. R., Ulbrich, I. M., Ng, N. L., Worsnop, D. R., Sun, Y., 2011. Understanding
640 atmospheric organic aerosols via factor analysis of aerosol mass spectrometry: A review. *Anal. Bioanal. Chem.* 401, 3045–
641 3067. <https://doi.org/10.1007/s00216-011-5355-y>

642 Huffman, J. A., Docherty, K. S., Aiken, A. C., Cubison, M. J., Ulbrich, I. M., DeCarlo, P. F., Jimenez, J. L., 2009. Chemically-
643 resolved aerosol volatility measurements from two megacity field studies. *Atmos. Chem. Phys.* 9, 7161–7182.
644 <https://doi.org/10.5194/acp-9-7161-2009>

645 Saha, P. K., Khlystov, A., Grieshop, A. P., 2014. Determining aerosol volatility parameters using a “dual thermodenuder”
646 system: Application to laboratory-generated organic aerosols. *Aerosol Sci. Technol.* 49, 620–632.
647 <https://doi.org/10.1080/02786826.2015.1056769>

648 Zhou, S., Collier, S., Jaffe, D. A., Briggs, N. L., Hee, J., Sedlacek III, A. J., Kleinman, L., & Lewis, K., 2017. Regional
649 influence of wildfires on aerosol chemistry in the western US and insights into atmospheric aging of biomass burning
650 organic aerosol. *Atmospheric Chemistry and Physics*, 17, 2477–2493. <https://doi.org/10.5194/acp-17-2477-2017>

651 Riipinen, I., Pierce, J. R., Donahue, N. M., Pandis, S. N., 2010. Equilibration time scales of organic aerosol inside
652 thermodenuders: Kinetics versus equilibrium thermodynamics. *Atmos. Environ.* 44, 597–607.
653 <https://doi.org/10.1016/j.atmosenv.2009.11.022>

654 Karnezi, E., Riipinen, I., Pandis, S. N., 2014. Measuring the atmospheric organic aerosol volatility distribution: a theoretical
655 analysis. *Atmos. Meas. Tech.* 7, 2953–2965. <https://doi.org/10.5194/amt-7-2953-2014>

656 Chen, Y., Wang, Z., Wang, Y., Zheng, X., Fu, P., Kawamura, K., Zhang, Y., 2021. Characterization of nitrogen-containing
657 organic aerosol in Guangzhou, China: seasonal variation, formation mechanism and source apportionment. *Atmos. Chem.
658 Phys.* 21, 4329–4344. <https://doi.org/10.5194/acp-21-4329-2021>

659 Hayes, P. L., Ortega, A. M., Cubison, M. J., Froyd, K. D., Zhao, Y., Cliff, S. S., ... Jimenez, J. L., 2013. Organic aerosol
660 composition and sources in Pasadena, California, during the 2010 CalNex campaign. *J. Geophys. Res. Atmos.* 118, 9233–
661 9257. <https://doi.org/10.1002/jgrd.50530>

662 Sun, Y., Jiang, Q., Wang, Z., Fu, P., Li, J., Yang, T., Yin, Y., 2011. Investigation of the sources and evolution processes of
663 severe haze pollution in Beijing in January 2013. *J. Geophys. Res. Atmos.* 119, 4380–4398.
664 <https://doi.org/10.1002/2014JD021641>

665 Baek, K. M., Park, E. H., Kang, H., Ji, M. J., Park, H. M., Heo, J & Kim, H., 2022. Seasonal characteristics of atmospheric
666 water-soluble organic nitrogen in PM2.5 in Seoul, Korea: Source and atmospheric processes of free amino acids and
667 aliphatic amines. *Science of the Total Environment*, 807, 150785. <https://doi.org/10.1016/j.scitotenv.2021.152335>

668 Rovelli, G., Miles, R. E. H., Reid, J. P., and Clegg, S. L.: Hygroscopic properties of aminium sulfate aerosols, *Atmos. Chem.
669 Phys.*, 17, 4369–4385, <https://doi.org/10.5194/acp-17-4369-2017>, 2017.

670 Ge, X., Wexler, A. S., Clegg, S. L., 2011. Atmospheric amines – Part I. A review. *Atmos. Environ.* 45, 524–546.
671 <https://doi.org/10.1016/j.atmosenv.2010.10.012>

672 He, J., Liu, H., Shan, P., Zhang, K., Qin, Y., & Liu, L. 2016. Supported-gas-membrane process for removal and recovery of
673 aliphatic amines from aqueous streams. *Chemical Engineering Science*, 144, 110–119.
674 <https://doi.org/10.1016/j.ces.2016.01.018>

675 You, Y., Renbaum-Wolff, L., Carreras-Sospedra, M., Dabdub, D., Bertram, A. K., Martin, S. T., et al., 2014. Images reveal
676 that amines promote the heterogeneous reaction of epoxides in model organic aerosols. *J. Phys. Chem. Lett.* 5, 3211–
677 3215. <https://doi.org/10.1021/jz501268k>

678 Yao, L., Wang, M. Y., Wang, X. K., Zhang, W. Q., Liu, Y., Li, L., et al., 2016. Atmospheric new particle formation from
679 sulfuric acid and amines in a Chinese megacity. *Sci. Bull.* 61, 939–945. <https://doi.org/10.1007/s11434-016-1083-0>

680 Kim, H., Zhang, Q., Sun, Y., Bae, G. N., Lee, B. E., Park, K., ... & Kim, Y. J. 2020. Measurement report: Characterization of
681 severe spring haze episodes and influences of long-range transport in the Seoul metropolitan area in March 2019.
682 *Atmospheric Chemistry and Physics*, 20(18), 11527–11545. <https://doi.org/10.5194/acp-20-11527-2020>

683 Jeon, J., Chen, Y., Kim, H., 2023. Influence of meteorology on emission sources and physicochemical properties of particulate
684 matter in Seoul, Korea during heating period. *Atmos. Environ.* 301, 119733.
685 <https://doi.org/10.1016/j.atmosenv.2023.119733>

686 Zhang, Q., Alfarra, M. R., Worsnop, D. R., Allan, J. D., Coe, H., Canagaratna, M. R., ... & Jimenez, J. L. 2005. Deconvolution
687 and quantification of hydrocarbon-like and oxygenated organic aerosols based on aerosol mass spectrometry.
688 *Environmental Science & Technology*, 39(13), 4938–4952. <https://doi.org/10.1021/es0485681>

689 Simoneit, B. R. T. 2002. Biomass burning – a review of organic tracers for smoke from incomplete combustion. *Applied
690 Geochemistry*, 17(3), 129–162. [https://doi.org/10.1016/S0883-2927\(01\)00061-0](https://doi.org/10.1016/S0883-2927(01)00061-0)

691 Cubison, M. J., Ortega, A. M., Hayes, P. L., Farmer, D. K., Day, D., Lechner, M. J., ... & Jimenez, J. L. 2011. Effects of aging
692 on organic aerosol from open biomass burning smoke in aircraft and laboratory studies. *Atmospheric Chemistry and*
693 *Physics*, 11(23), 12049–12064. <https://doi.org/10.5194/acp-11-12049-2011>

694 Xu, L., Williams, L. R., Young, D. E., Allan, J. D., Coe, H., Massoli, P., Fortner, E., Chhabra, P., Herndon, S., Brooks, W. A.,
695 Jayne, J. T., Worsnop, D. R., Aiken, A. C., Liu, S., Gorkowski, K., Dubey, M. K., Fleming, Z. L., Visser, S., Prévôt, A.
696 S. H., Ng, N. L., 2016. Wintertime aerosol chemical composition, volatility, and spatial variability in the Greater London
697 Area. *Atmos. Chem. Phys.* 16, 1139–1160. <https://doi.org/10.5194/acp-16-1139-2016>

698 Feng, T., Wang, Y., Hu, W., Zhu, M., Song, W., Chen, W., ... Wang, X., 2023. Impact of aging on the sources, volatility, and
699 viscosity of organic aerosols in Chinese outflows. *Atmos. Chem. Phys.* 23, 611–636. <https://doi.org/10.5194/acp-23-611-2023>

700 701 Scott, W. D., & Cattell, F. C. R. 1979. Vapor pressure of ammonium sulfates. *Atmospheric Environment* (1967), 13(6), 987–
702 1000. [https://doi.org/10.1016/0004-6981\(79\)90174-4](https://doi.org/10.1016/0004-6981(79)90174-4)

703 704 Donahue, N. M., Robinson, A. L., Pandis, S. N., 2009. Atmospheric organic particulate matter: From smoke to secondary
705 organic aerosol. *Atmos. Environ.* 43, 94–106. <https://doi.org/10.1016/j.atmosenv.2008.09.055>

706 Ehn, M., Thornton, J. A., Kleist, E., Sipilä, M., Junninen, H., Pullinen, I., ... & Kulmala, M. 2014. A large source of low-
707 volatility secondary organic aerosol. *Nature*, 506(7489), 476–479. <https://doi.org/10.1038/nature13032>

708 Kroll, J. H., Smith, J. D., Che, D. L., Kessler, S. H., Worsnop, D. R., Wilson, K. R., 2009. Measurement of fragmentation and
709 functionalization pathways in the heterogeneous oxidation of oxidation organic aerosol. *Environ. Sci. Technol.* 43, 7826–
7833. <https://doi.org/10.1021/es901683r>

710 Xu, L., Williams, L.R., Young, D.E., Allan, J.D., Coe, H., Massoli, P., Fortner, E., Chhabra, P., Herndon, S., Brooks, W.A.,
711 et al., 2016. Wintertime aerosol chemical composition, volatility, and spatial variability in the greater London area. *Atmos.*
712 *Chem. Phys.* 16, 1139–1160. <https://doi.org/10.5194/acp-16-1139-2016>

713 Cao, L.-M., Huang, X.-F., Li, Y.-Y., Hu, M., He, L.-Y., 2018. Volatility measurement of atmospheric submicron aerosols in
714 an urban atmosphere in southern China. *Atmos. Chem. Phys.* 18, 1729–1743. <https://doi.org/10.5194/acp-18-1729-2018>

715 Xu, W., Xie, C., Karnezi, E., Zhang, Q., Wang, J., Pandis, S.N., Ge, X., Zhang, J., An, J., Wang, Q., et al., 2019. Summertime
716 aerosol volatility measurements in Beijing, China. *Atmos. Chem. Phys.* 19, 10205–10216. <https://doi.org/10.5194/acp-19-10205-2019>

717 718 Allan, J. D., Alfarra, M. R., Bower, K. N., Williams, P. I., Gallagher, M. W., Jimenez, J. L., McDonald, A. G., Nemitz, E.,
719 Canagaratna, M. R., and Coe, H.: Quantitative sampling using an Aerodyne aerosol mass spectrometer—2. Measurements
720 of fine particulate chemical composition in two U.K. cities, *J. Geophys. Res.-Atmos.*, 108, 4091, 2003,
721 <https://doi.org/10.1029/2002JD002359>.

722 Berndt, T., Richters, S., Jokinen, T., et al.: Hydroxyl radical-induced formation of highly oxidized organic compounds, *Nat.*
723 *Commun.*, 7, 13677, 2016, <https://doi.org/10.1038/ncomms13677>.

725 Bianchi, F., Kurtén, T., Riva, M., et al.: Highly oxygenated organic molecules (HOM) from gas-phase autoxidation involving
726 peroxy radicals: A key contributor to atmospheric aerosol, *Chem. Rev.*, 119, 3472–3509, 2019,
727 <https://doi.org/10.1021/acs.chemrev.8b00395>.

728 Brown, S. S. and Stutz, J.: Nighttime radical observations and chemistry, *Chem. Soc. Rev.*, 41, 6405–6447, 2012,
729 <https://doi.org/10.1039/C2CS35181A>.

730 Canagaratna, M. R., Jayne, J. T., Jimenez, J. L., et al.: Chemical and microphysical characterization of ambient aerosols with
731 the Aerodyne aerosol mass spectrometer, *Mass Spectrom. Rev.*, 26, 185–222, 2007, <https://doi.org/10.1002/mas.20115>.

732 Chhabra, P. S., Ng, N. L., Canagaratna, M. R., et al.: Elemental composition and oxidation of chamber organic aerosol, *Atmos.*
733 *Chem. Phys.*, 11, 8827–8841, 2011, <https://doi.org/10.5194/acp-11-8827-2011>.

734 D’Ambro, E. L., Schobesberger, S., Gaston, C. J., et al.: Molecular composition and volatility of isoprene photochemical
735 oxidation secondary organic aerosol under low- and high-NO_x conditions, *Atmos. Chem. Phys.*, 17, 159–174, 2017,
736 <https://doi.org/10.5194/acp-17-159-2017>.

737 Donahue, N. M., Epstein, S. A., Pandis, S. N., and Robinson, A. L.: A two-dimensional volatility basis set – Part 1: Organic-
738 aerosol mixing thermodynamics, *Atmos. Chem. Phys.*, 11, 3303–3318, 2011, <https://doi.org/10.5194/acp-11-3303-2011>.

739 Faulhaber, A. E., Thomas, B. M., Jimenez, J. L., et al.: Characterization of a thermodenuder–particle beam mass spectrometer
740 system for the study of organic aerosol volatility and composition, *Atmos. Meas. Tech.*, 2, 15–31, 2009,
741 <https://doi.org/10.5194/amt-2-15-2009>.

742 Ge, X., Wexler, A. S., and Clegg, S. L.: Atmospheric amines – Part III: Photochemistry and toxicity, *Atmos. Environ.*, 45,
743 561–591, 2011, <https://doi.org/10.1016/j.atmosenv.2010.11.050>.

744 Gil, J., Lee, Y., and Kim, Y. P.: Characteristics of HONO and its impact on O₃ formation in the Seoul Metropolitan Area
745 during KORUS-AQ, *Atmos. Environ.*, 246, 118032, 2021, <https://doi.org/10.1016/j.atmosenv.2020.118032>.

746 Han, K.-M., Kim, D.-G., Kim, J., et al.: Crop residue burning emissions and impact on particulate matter over South Korea,
747 *Atmosphere*, 13, 559, 2022, <https://doi.org/10.3390/atmos13040559>.

748 Hanson, D. R., McMurry, P. H., Jiang, J., et al.: Ambient pressure proton transfer mass spectrometry: detection of amines and
749 ammonia, *Environ. Sci. Technol.*, 45, 8881–8888, 2011, <https://doi.org/10.1021/es2018817>.

750 Hennigan, C. J., Sullivan, A. P., Collett, J. L., Jr., and Robinson, A. L.: Levoglucosan stability in biomass burning particles
751 exposed to hydroxyl radicals, *Geophys. Res. Lett.*, 37, L09806, 2010, <https://doi.org/10.1029/2010GL043088>.

752 Huffman, J. A., Ziemann, P. J., Jayne, J. T., et al.: Development and characterization of a fast-stepping thermodenuder for
753 chemically resolved aerosol volatility measurements, *Aerosol Sci. Technol.*, 42, 395–407, 2008,
754 <https://doi.org/10.1080/02786820802104981>.

755 Kim, K., Park, R., Lee, Y., et al.: An investigation into atmospheric nitrous acid (HONO) and its sources in East Asia, *Atmos.*
756 *Chem. Phys.*, 24, 12575–12593, 2024, <https://doi.org/10.5194/acp-24-12575-2024>.

757 Kroll, J. H. and Seinfeld, J. H.: Chemistry of secondary organic aerosol: Formation and evolution of low-volatility organics in
758 the atmosphere, *Atmos. Environ.*, 42, 3593–3624, 2008, <https://doi.org/10.1016/j.atmosenv.2008.01.003>.

759 Kroll, J., Donahue, N., Jimenez, J., et al.: Carbon oxidation state as a metric for describing the chemistry of atmospheric
760 organic aerosol, *Nat. Chem.*, 3, 133–139, 2011, <https://doi.org/10.1038/nchem.948>.

761 Kwon, S., Won, S. R., Lim, H. B., et al.: Relationship between PM1.0 and PM2.5 in urban and background areas of the
762 Republic of Korea, *Atmos. Pollut. Res.*, 14, 101858, 2023, <https://doi.org/10.1016/j.apr.2023.101858>.

763 Lamb, K. D., Kim, B.-G., and Kim, S.-W.: Estimating source-region influences on black carbon in South Korea using the
764 BC/CO ratio, *J. Geophys. Res.-Atmos.*, 123, 11, 2018, <https://doi.org/10.1029/2018JD029257>.

765 Lambe, A. T., Onasch, T. B., Massoli, P., et al.: Transitions from Functionalization to Fragmentation Reactions of Laboratory
766 Secondary Organic Aerosol (SOA) Generated from the OH Oxidation of Alkane Precursors, *Environ. Sci. Technol.*, 46,
767 5430–5437, 2012, <https://doi.org/10.1021/es300274t>.

768 López-Hilfiker, F. D., Mohr, C., Ehn, M., et al.: A novel method for online analysis of gas and particle composition: description
769 and evaluation of a Filter Inlet for Gases and AEROSols (FIGAERO), *Atmos. Meas. Tech.*, 7, 983–1001, 2014,
770 <https://doi.org/10.5194/amt-7-983-2014>.

771 López-Hilfiker, F. D., Mohr, C., Ehn, M., et al.: Molecular composition and volatility of organic aerosol in the Southeastern
772 U.S. using FIGAERO-CIMS with comparison to AMS, *Environ. Sci. Technol.*, 50, 2200–2209, 2016,
773 <https://doi.org/10.1021/acs.est.5b04769>.

774 Mao, J., Wang, L., Lu, C., et al.: High-resolution modeling of gaseous methylamines over a polluted region in China: source-
775 dependent emissions and implications of spatial variations, *Atmos. Chem. Phys.*, 18, 7933–7950, 2018,
776 <https://doi.org/10.5194/acp-18-7933-2018>.

777 Matsui, H., Koike, M., Kondo, Y., et al.: An estimation of the organic aerosol component in PM2.5 using AMS and CMB
778 models, *J. Geophys. Res.-Atmos.*, 114, D21203, 2009, <https://doi.org/10.1029/2009JD012170>.

779 Nault, B. A., Campuzano-Jost, P., Day, D. A., et al.: Secondary organic aerosol production from local emissions dominates
780 over Seoul during KORUS-AQ, *Atmos. Chem. Phys.*, 18, 17769–17800, 2018, <https://doi.org/10.5194/acp-18-17769-2018>.

782 Nielsen, C. J., Herrmann, H., and Weller, C.: Atmospheric chemistry and environmental impact of the use of amines in carbon
783 capture and storage (CCS), *Chem. Soc. Rev.*, 41, 6684–6704, 2012, <https://doi.org/10.1039/C2CS35059A>.

784 Slater, E. J., Gkatzolias, D., Wang, Y., et al.: Elevated levels of OH observed in haze events during wintertime Beijing, *Atmos.*
785 *Chem. Phys.*, 20, 14847–14871, 2020, <https://doi.org/10.5194/acp-20-14847-2020>.

786 Sun, Y., Zhang, Q., Schwab, J. J., et al.: Characterization of the sources and properties of organic aerosol from AMS
787 measurements during a winter campaign in Beijing, China, *Atmos. Chem. Phys.*, 10, 8951–8971, 2010,
788 <https://doi.org/10.5194/acp-10-8951-2010>.

789 Tiszenkel, L., Flynn, J. H., and Lee, S.-H.: Measurement report: Urban ammonia and amines in Houston, Texas, *Atmos. Chem.*
790 *Phys.*, 24, 11351–11363, 2024, <https://doi.org/10.5194/acp-24-11351-2024>.

791 Yoo, H., Lee, H., and Kim, Y. P.: Insights from single-particle analysis: submicron aerosol composition in Seoul during
792 KORUS-AQ, *Atmos. Chem. Phys.*, 24, 853–872, 2024, <https://doi.org/10.5194/acp-24-853-2024>.

793 Ziemann, P. J. and Atkinson, R.: Kinetics, products, and mechanisms of secondary organic aerosol formation from gas-phase
794 reactions of organic compounds, *Chem. Soc. Rev.*, 41, 6582–6605, 2012, <https://doi.org/10.1039/C2CS35122F>.

795 Paciga, A., Young, D. E., Ward, M. W., et al.: Volatility of organic aerosol and its components in the megacity of Paris, *Atmos.*
796 *Chem. Phys.*, 16, 2013–2031, 2016, <https://doi.org/10.5194/acp-16-2013-2016>.

797 Ge, X., Wexler, A. S., and Clegg, S. L.: Atmospheric amines – Part II. Thermodynamic properties and gas-particle partitioning,
798 *Atmos. Chem. Phys.*, 11, 55–69, 2011, <https://doi.org/10.5194/acp-11-55-2011>.

799 Xu, W., Sun, Y., Wang, Q., et al.: Seasonal characterization of organic nitrogen in atmospheric aerosols using high-resolution
800 aerosol mass spectrometry in Beijing, China, *ACS Earth Space Chem.*, 1, 649–658, 2017,
801 <https://doi.org/10.1021/acsearthspacechem.7b00106>.

802 Sun, Y. L., Zhang, Q., Schwab, J. J., et al.: Characterization of the sources and processes of organic and inorganic aerosols in
803 New York City with a high-resolution time-of-flight aerosol mass spectrometer, *Atmos. Chem. Phys.*, 11, 1581–1602,
804 2011, <https://doi.org/10.5194/acp-11-1581-2011>.

805 Saarikoski, S., Carbone, S., Decesari, S., et al.: Chemical characterization of springtime submicrometer aerosol in Po Valley,
806 Italy, *Atmos. Chem. Phys.*, 12, 8401–8421, 2012, <https://doi.org/10.5194/acp-12-8401-2012>.

807 Silva, P. J., Erupe, M. E., Price, D., et al.: Trimethylamine as precursor to secondary organic aerosol formation via nitrate
808 radical reaction in the atmosphere, *Environ. Sci. Technol.*, 42, 4689–4696, 2008, <https://doi.org/10.1021/es703016v>